Institute of Technology and Engineering (ITE)

Optimization of a 900 MHz Elliptical Dipole Antenna for a GPR Monitoring System

Rati Chkhetia, Forschungszentrum Jülich,
Institute of Technology and Engineering (ITE)

Lea Schreckenberg, Forschungszentrum Jülich,
Peter Grünberg Institute – Integrated Computing Architectures (ICA|PGI-4)

Achim Mester, Forschungszentrum Jülich,
Institute of Technology and Engineering (ITE)

Egon Zimmermann, Forschungszentrum Jülich,
Institute of Technology and Engineering (ITE)

Ghaleb Natour, Forschungszentrum Jülich,
Institute of Technology and Engineering (ITE)

Jül-4450

Mitglied der Helmholtz-Gemeinschaft

JÜLICH
Forschungszentrum

Berichte des Forschungszentrums Jülich
Jül-4450 · ISSN 0944-2952
Institute of Technology and Engineering (ITE)

Vollständig frei verfügbar über das Publikations-
portal des Forschungszentrums Jülich (JuSER)
unter www.fz-juelich.de/zb/openaccess

Forschungszentrum Jülich GmbH · 52425 Jülich
Zentralbibliothek, Verlag
Tel.: 02461 61-5220 · Fax: 02461 61-6103
zb-publikation@fz-juelich.de
www.fz-juelich.de/zb

Institute of Technology and Engineering (ITE)

Optimization of a 900 MHz Elliptical Dipole Antenna for a GPR Monitoring System

Rati Chkhetia*, Forschungszentrum Jülich,
Institute of Technology and Engineering (ITE)

Lea Schreckenberg, Forschungszentrum Jülich,
Peter Grünberg Institute – Integrated Computing Architectures (ICA|PGI-4)

Achim Mester, Forschungszentrum Jülich,
Institute of Technology and Engineering (ITE)

Egon Zimmermann, Forschungszentrum Jülich,
Institute of Technology and Engineering (ITE)

Ghaleb Natour, Forschungszentrum Jülich,
Institute of Technology and Engineering (ITE)

*This work was supported by Shota Rustaveli National Science Foundation of Georgia (SRNSFG) JFZ-23-021

Optimization of a 900 MHz Elliptical Dipole Antenna for a GPR Monitoring System

Rati Chkhetia[1, *], Lea Schreckenberg[2], Achim Mester[1], Egon Zimmermann[1], Ghaleb Natour[1,3]

1. Forschungszentrum Jülich, Institute of Technology and Engineering (ITE), Jülich, Germany
2. Forschungszentrum Jülich, Peter Grünberg Institute - Integrated Computing Architectures (ICA | PGI-4), Jülich, Germany
3. RWTH Aachen University, Faculty of Mechanical Engineering (ISF), Aachen, Germany

*This work was supported by Shota Rustaveli National Science Foundation of Georgia (SRNSFG) JFZ-23-021

Abstract

The antenna is a critical component determining the performance of a Ground-Penetrating Radar (GPR) system, directly impacting its signal-to-noise ratio (SNR), resolution, and survey depth. A custom GPR currently in development at Institute of Technology and Engineering (ITE) at Forschungszentrum Jülich GmbH requires antennas with optimal performance in the frequency range of 450 MHz to 1350 MHz, linear phase characteristics and uniform radiation for an angle of approximately 90 degrees.

This paper presents the analysis and optimization of a custom planar elliptical dipole. The existing shrinked antenna design was evaluated. Scattering parameter measurements were performed alongside simulations to validate the accuracy of the numerical model and determine the feasibility of optimization.

Using the CST Studio Suite simulation environment, various geometrical parameters were analyzed to determine their impact on the reflection coefficient and radiation patterns. Sensitivity analysis indicated that changing the size constraints was necessary for better efficiency. Within the redefined but still compact constraints, optimization was performed to maximize the operating bandwidth. The resulting optimized design maintains a reflection coefficient better than –10 dB in the 900-1350 MHz range. Due to physical size limitations, the reflection coefficient gradually degrades below 900 MHz, yielding >-5 dB at 450 MHz.

Table of Contents

1 Introduction

Comprehensive measurements of soil characteristics are required for research in the field of sustainable agriculture to develop innovative strategies for crop yield optimization, efficient nutrient application, and sustainable soil use [1].

Ground-penetrating radar (GPR) is a non-destructive geophysical method used to investigate subsurface properties. It operates by transmitting electromagnetic waves into the ground, which experience time delays and attenuation based on the varying electrical characteristics of the medium through which they propagate. The returning signals are captured by receiving antennas and processed to generate images of subsurface structures. GPR generally operates within a frequency range of 10 MHz to 3600 MHz [2]. There is a trade-off in this selection: lower frequencies allow for deeper penetration, while higher frequencies provide greater resolution. Due to its non-invasive nature and ability to perform high-speed, high-resolution measurements, GPR is often preferred over other geophysical methods. It is employed in a wide variety of applications, including agriculture, civil engineering, archaeology and space exploration ([3], [4], [5], [6]).

GPR systems are categorized into two configurations based on antenna-surface coupling [7]. In case of air-coupled systems, there is some space between the antennas and ground. This allows more mobility, since the antennas can be mounted on a vehicle and moved quickly to scan an area. In contrast, ground-coupled GPR antennas are directly in contact with the surface. Because of this, energy is transferred to the ground more efficiently, allowing deeper penetration. Depending on coupling, different types of antennas are used. For air-coupled GPR applications horn antennas are more advantageous because of their narrow beam width and thereby achieved gain, while ground-coupled systems utilize planar Printed Circuit Board (PCB) antennas because of their linear phase characteristics [8].

According to Pathirana et al [2], GPR uses three primary data acquisition modes depending on the application and the frequency range:

1. **Reflection profiling** – The Tx and Rx antennas maintain a constant distance from one another as they are moved along the surface. From the collected sub-surface reflections, a two-dimensional cross-section is generated.
2. **Velocity-sounding** – Relationship between wave travel time and antenna separation is analyzed to estimate the velocity of radar waves through subsurface materials. It employs two techniques:
    - **Common Mid-Point (CMP)** – the Tx and Rx antennas are moved apart in opposite directions, maintaining equal distances from a fixed central point.
    - **Wide-Angle Reflection and Refraction (WARR)** – One antenna remains at a specific location, while the second antenna is moved in fixed steps to increase the separation.
3. **Transillumination** – The Tx and Rx antennas are positioned on opposite sides of the medium under investigation. This can be done in three different configurations:
    - **Zero-Offset Profiling (ZOP)** – both antennas are moved simultaneously at consistent depth intervals.

- **Multi-Offset Gathering (MOG)** – One antenna remains fixed at a specific depth while the other is moved to multiple positions.
- **Vertical Reflection Profiling (VRP)** – The Tx operates from surface, while the Rx is placed into a borehole at different depths.

Propagation of the electromagnetic wave is influenced by three electrical parameters of the medium: dielectric permittivity (ε), electrical conductivity (σ) and magnetic permeability (μ).

Dielectric permittivity quantifies how much the material is polarized in the presence of an electric field. It is expressed in farads per meter (F/m) and often defined with relative permittivity $\varepsilon_r = \frac{\varepsilon}{\varepsilon_0}$, where ε_0≈8.854×10−12 F/m is the dielectric permittivity of vacuum. Variations in ε in the subsurface cause reflections which are detected by GPR systems when mapping structures [7]. Concentration of water in the soil significantly impacts dielectric permittivity. Water has a relative permittivity of about 81, whereas most dry soil components have permittivities below 10. This contrast makes it possible to use GPR systems for estimating soil water content [1].

Electrical conductivity, measured in siemens per meter (S/m) represents a material's ability to conduct electric current and is the inverse of electrical resistivity (Ohm/m). It determines the attenuation of the electromagnetic waves as they travel through a medium. Materials with high conductivity cause significant attenuation and limit the depth to which the radar waves can penetrate.

The unit for magnetic permeability is Henries per meter (H/m). It is a measure of material's ability to support the formation of a magnetic field. Just like permittivity, permeability is often expressed in terms of its relative value: $\mu_r = \frac{\mu}{\mu_0}$, where $\mu_0 = 4\pi \times 10^{-7}$, permeability of vacuum. For GPR applications in soil sciences, variations in magnetic permeability are negligible compared to dielectric permittivity and electrical conductivity. Therefore, relative permeability μ_r is approximated to be 1 (same as free space). Exceptions are cases when the material under investigation is ferromagnetic [7].

The velocity of an electromagnetic wave traveling in a dielectric medium can be calculated by the following equation:

$$v = \frac{c}{\sqrt{\varepsilon_r \mu_r}} \tag{1}$$

If we assume that μ_r is constant, the velocity is determined by the dielectric permittivity.

Attenuation of an electromagnetic wave, as can be seen from the equation 2, is directly proportional to electrical conductivity of the material.

$$\alpha = \frac{1}{2}\sigma\sqrt{\frac{\mu}{\varepsilon}} \tag{2}$$

Equations 1 and 2 are valid for a certain frequency range referred to as "GPR plateau", which is usually 1-1000 MHz [9]. In this range, electrical parameters of the soil are independent from the frequency.

The selection of the frequencies included in the transmitted waveform is important while designing GPR systems, since it determines resolution and depth of penetration of the radar.

The minimum distance between two targets resolved by a radar is defined by the following equation [10]:

$$\Delta R = \frac{v}{2B} \tag{3}$$

, where v is propagation velocity of an electromagnetic wave and B is bandwidth of the transmitted waveform. Bandwidth in this case refers to the range of frequencies that a waveform occupies and is defined as the difference between the highest and lowest frequencies - $f_{max} - f_{min}$. Increasing the bandwidth of the transmitted waveform decreases minimum non-ambiguous distance, leading to better resolution. However, higher frequencies experience more attenuation and have lower depth of penetration. Therefore, the operating bandwidth of a GPR system is limited to a certain range, based on the application.

The requirements for antennas used in GPR systems are usually stringent. Linear polarization is typically employed in order to resolve horizontal structures in the soil. To accommodate the necessary resolution and depth, the antenna must cover a wide frequency range [8]. Minimum fractional bandwidth of 100% is a common requirement [11]. A balance must be struck between penetration depth and spatial resolution. For ground-coupled GPRs, soil is in the reactive near-field region ($r < \lambda/2\pi$), therefore it changes the characteristics of the antenna. This effect must be accounted for in the antenna design [11]. In addition, the antennas should have good impedance matching, be linear in phase, and avoid side lobes. Some common dipole antennas are shown in Figure 1. The focus in this paper is on the elliptical dipole antenna (f).

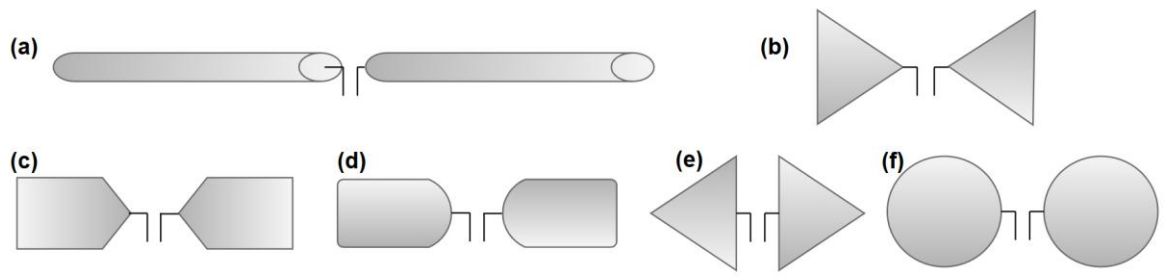

Figure 1. Typical antenna designs for GPR systems, including (a) low-bandwidth variants and (b)-(f) different approaches to increase bandwidth and reduce side-lobes. Illustration adapted from [12].

While a standard dipole antenna (Figure 1a) offers a simple design and linear polarization, it has a narrow bandwidth with its centre frequency determined by its length. To broaden the bandwidth, the conductor's volume must be increased. In planar PCB designs, where thickening the conductor is not feasible, dipole arms are

instead widened into triangular shapes to form a bow-tie antenna (Figure 1b). Although the bow-tie antenna achieves a wider bandwidth, the specific geometry allows for varying current path lengths. This can introduce unwanted ringing (also referred to as “side lobes”). Designs with rounded corners, especially the elliptical dipole variant (Figure 1f) have wide bandwidth and low ringing [12].

At Forschungszentrum Jülich GmbH a Scalable, Multi-Channel Tomography GPR (SMUCT-GPR) [13] system is being developed for the Agricultural Simulator (AgraSim) [14] facility consisting of lysimeters, which are cylindrical containers filled with soil. The GPR system is designed to comprise more than 2,000 antennas positioned around the lysimeter. Each antenna can be operated as both a transmitter, sending electromagnetic waves into the lysimeter, and a receiver. As these waves travel through the soil, their properties are altered depending on changes in the soil's electrical properties, resulting in delays and attenuation. Distributions of electrical conductivity and permittivity within the lysimeter are estimated by analysing the received signals using algorithms such as full waveform inversion [15]. Given the large number of antennas and the wide bandwidth requirements (450–1350 MHz), it is crucial to optimize the antenna characteristics.

This paper presents progress on antenna design and optimization. The SMUCT-GPR project uses custom elliptical dipole antennas designed to provide a broad bandwidth while remaining compact. Because of size limitations, we optimized the antenna geometry with a special focus on the best performance within the desired frequency range for a rather small form factor.

2 Materials and Methods

2.1 Geometric Dimensions and Initial Antenna Design

The variables representing geometric dimensions of the elliptical dipole antenna are illustrated in Figure 2a. D_x and D_y are the diameters of the elliptical elements, l – separation between them, W_{sub} – substrate width, L_{sub} – substrate length, h - substrate thickness. 1mm margin between conducting elements and PCB substrate edge is established to avoid copper delamination.

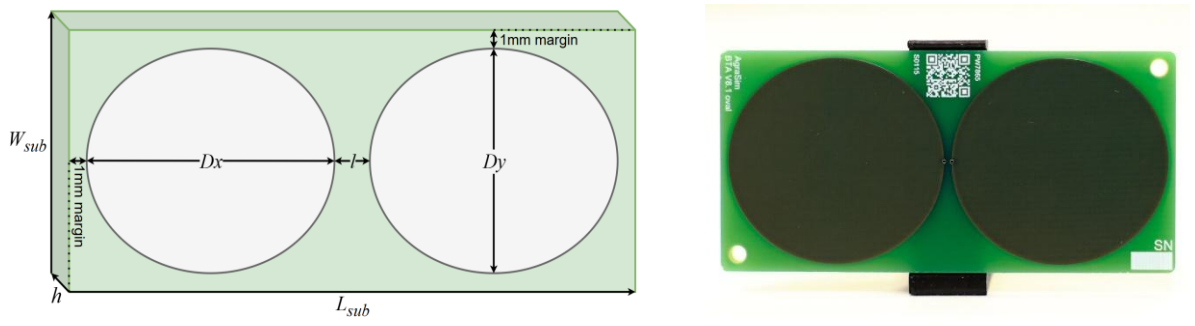

(a) (b)

Figure 2. Antenna modelling details: (a) Perspective view of the elliptical dipole PCB model with dimensions. (b) Photograph of the fabricated elliptical dipole PCB.

For initial tests of the theoretical research and to verify the simulation approach, we manufactured an initial elliptical bow-tie antenna (Figure 2b).

The antenna is implemented on a double-sided FR-4 PCB with substrate dimensions of 58.5 mm x 28.5 mm x 1.5 mm. The radiating structure consists of two elliptical elements on the top layer, defined by diameters $D_x = 27.7\ \mathrm{mm}$ and $D_y = 26.5\ \mathrm{mm}$, with a separation l of 1.0 mm. These elements are connected via conductive through-holes (vias) to the balun network, which is located on the bottom layer of the PCB (Figure 3b). For the balun, we use a Mini-Circuits TC1-1-13MG2 device. To connect the antenna to the measurement system via coaxial cables, a Molex MCRF SMD connector is placed on each antenna.

2.2 Numerical Simulations

The numerical analysis and optimization of the antenna design were conducted using the CST Studio Suite 2025 software. The simulations utilized the time-domain solver based on Finite Integration Technique (FIT). The computational domain was discretized using a hexahedral mesh.

The geometry of the current design was modeled based on physical dimensions of the PCB. The conductive components of the antenna, including the radiating elliptical elements, ports and vias, were approximated as perfect electric conductors (PEC). The substrate was defined as FR-4 material with a relative permittivity (ε_r) of 4.3.

Another important aspect of the modeling was the feed network, which includes a balun transformer. To account for the balun's frequency-dependent behavior without modeling its complex internal geometry, the manufacturer's S-parameter data were imported and integrated into the simulation environment. Additionally, a small conductor plate was modelled to serve as a ground reference for the balun's multipin element.

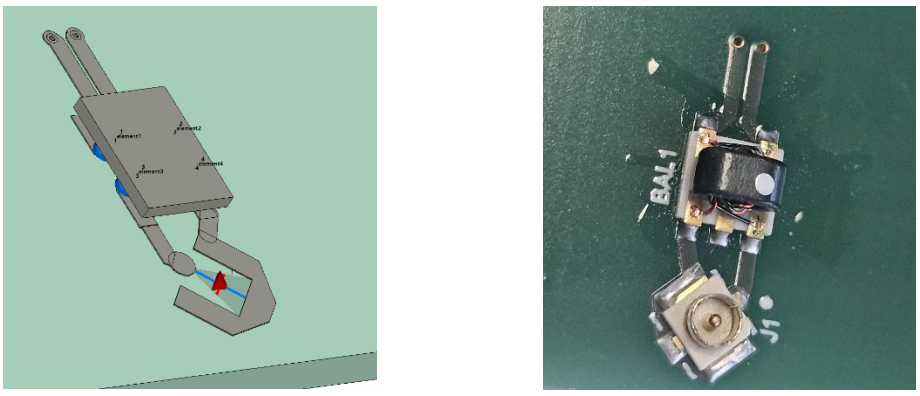

(a) **(b)**

Figure 3. Antenna modelling details: (a) View of the port on the back of the PCB, showing common conductor plate for the balun multipin element and the discrete input port indicated by the red arrow. (b) Photograph of the physical port and balun assembly on the back of the PCB.

To characterize the radiation properties of the antenna, far-field monitors were defined at three frequencies spanning the operational bandwidth of the GPR system: the lower bound (450 MHz), the center frequency (900 MHz) and the upper bound (1350 MHz). The far field gain patterns were analyzed in two planes: the E-plane, defined as the x-z plane and the H-plane, defined as the y-z plane. The orientation of the antenna model with respect to the coordinate system is depicted in Figure 4.

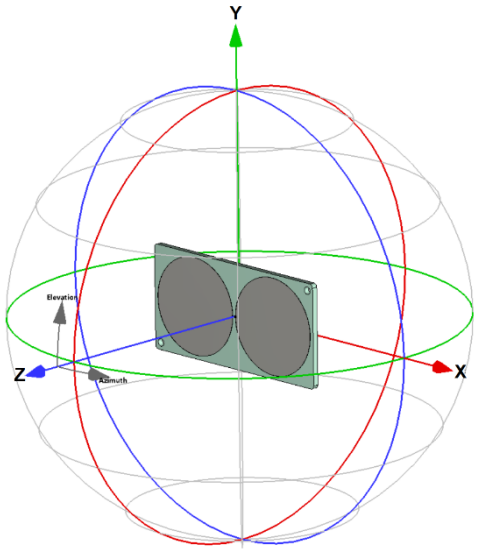

Figure 4. Antenna model displayed within the coordinate system, illustrating orientation used for defining the E-plane (x-z) and H-plane (y-z).

We distinguish between two different types of numerical studies: (1) parameter sweeps that aim at identifying the parameters required to tune the antenna to the desired operating bandwidth and (2) optimization to find the overall optimal antenna design.

2.3 Measurement Procedure

The S-parameters of the fabricated antenna prototypes were measured experimentally. The characterization was performed in a controlled electromagnetic environment using high-frequency instrumentation and a custom mechanical testing rig.

Scattering parameters were acquired using a Keysight E5071C ENA Vector Network Analyzer (VNA). Prior to measurements, the instrument was calibrated to compensate for cable length delay and losses. The calibration procedure was performed using Open, Short and Through standards to establish a reference at the end of the coaxial SMA cables. As described in the chapter 2.1 and Figure 3b, the physical interface to the antenna PCB utilizes a Molex MCRF male surface mount (SMD) connector, which requires a “pigtail” adapter for connection to the VNA’s cables. This adapter introduces additional electrical length and attenuation not present in the calibration plane. To compensate for these effects, a port extension was applied within the VNA settings.

A custom mechanical fixture was used to secure the antennas during testing. As shown in Figure 5, the setup has low-permittivity foam blocks (white) to support the antenna PCB. The fixture also allows variable distance adjustment between transmitting and receiving antennas for 2-port measurements.

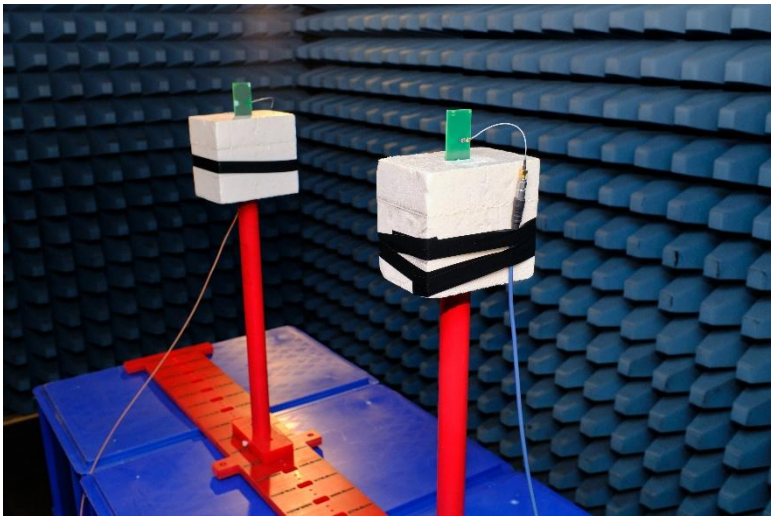

Figure 5. Photograph of a measurement setup in the anechoic chamber. Elliptical dipole antenna with a “pigtail” adapter is mounted on a stand and connected to a Vector Network Analyzer (VNA) with a coaxial cable.

3 Results

3.1 Scattering Parameters of the Initial Antenna Design

The performance of the fabricated elliptical dipole PCB was validated through both single port (S_{11}) and two-port (S_{11}, S_{12}, S_{21}, S_{22}) measurements. The reflection coefficient was first evaluated for a single antenna. Figure 6 presents the comparison between the simulated and measured S_{11} amplitude and phase responses. The measured amplitude exhibits a slight shift in the resonant frequency compared to the simulation. This is likely attributed to manufacturing tolerances in the FR-4 substrate (permittivity variations). However, the overall profile of the curve shows agreement with the numerical simulation. The phase response confirms the effectiveness of the port extension correction.

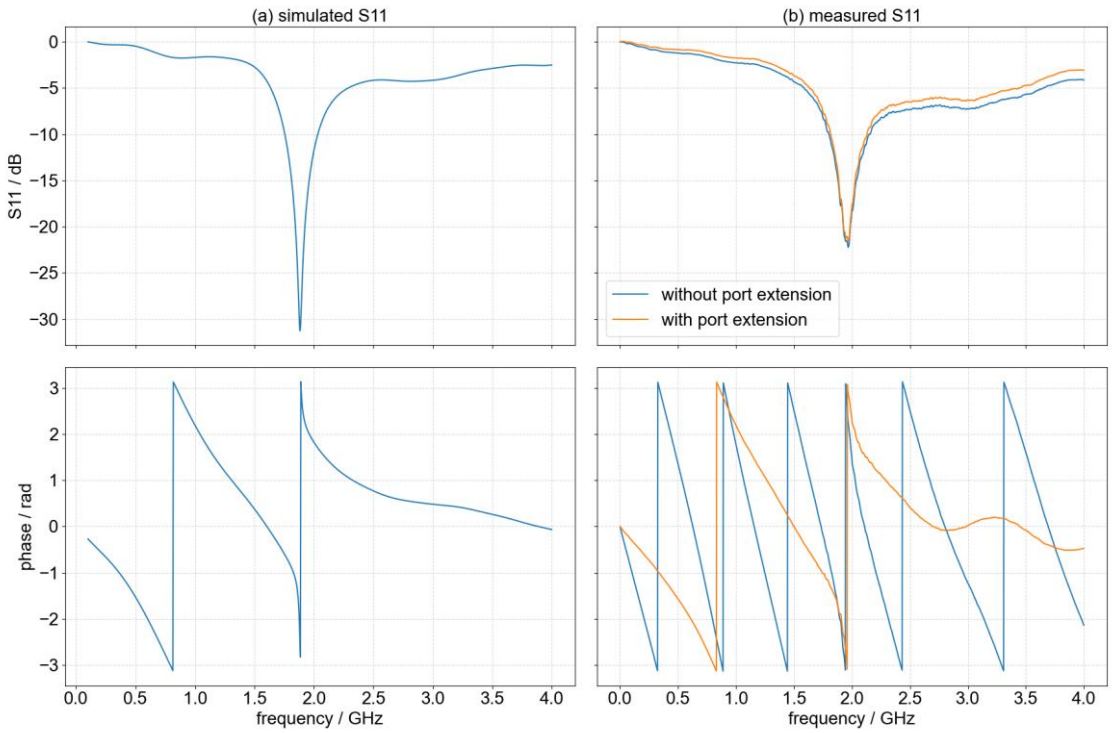

Figure 6. Comparison of simulated and measured reflection coefficient (S_{11}).

Two-port measurement was conducted with two antennas facing each other at 50 cm. A corresponding simulation model was created in CST. The results, displayed in Figure 7, compare the full S-parameter matrix. The transmission coefficients show that radiation is peaking near the resonant frequency, where the efficiency is highest. The measured data exhibits irregular noise peaks below –60 dB in the lower frequency band (approximately 0-0.8 GHz). This could be because the antenna is electrically small and highly inefficient in this range, resulting in received signal levels that approach the noise floor of the VNA.

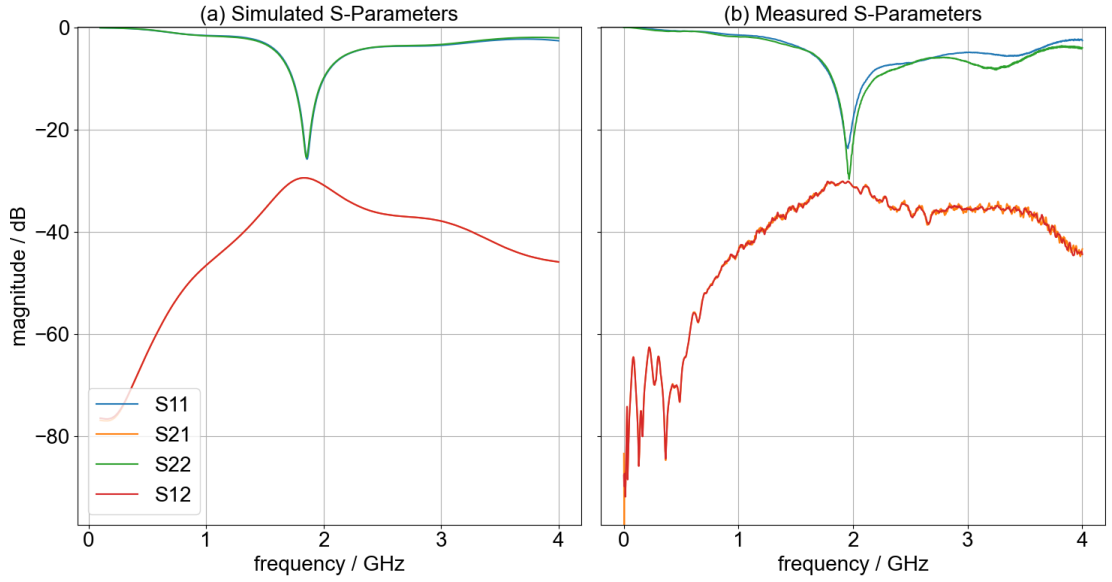

Figure 7. Comparison of measured and simulated 2-port scattering parameters.

3.2 Parameter Analysis

3.2.1 PCB Thickness

To study the effect of capacitive influences between the two layers, a parameter sweep was performed across the thickness h of the PCB substrate. This analysis involved incrementally increasing the substrate thickness (and consequently the via length) to observe changes in the antenna characteristics.

(a) (b)

Figure 8. Antenna models with different PCB thickness: (a) h=1.5 mm, (b) h=10 mm.

The simulated reflection coefficient (S_{11}) for h ranging from 1.5 mm to 10 mm is presented in Figure 9. The results show a correlation between h and resonant frequency in the range between 1.5 and 2 GHz. As the thickness increases, the frequency shifts downward. The profile of the curve also undergoes changes: At smaller h of 1.5 mm, the antenna exhibits sharper dip and better matching (-32 dB) at resonance. As h increases, the bandwidth gets broader, however, matching performance is degraded. Thicker configurations (h =7.5 mm and h =10 mm) exhibit a higher-order resonant modes above 3.5 GHz.

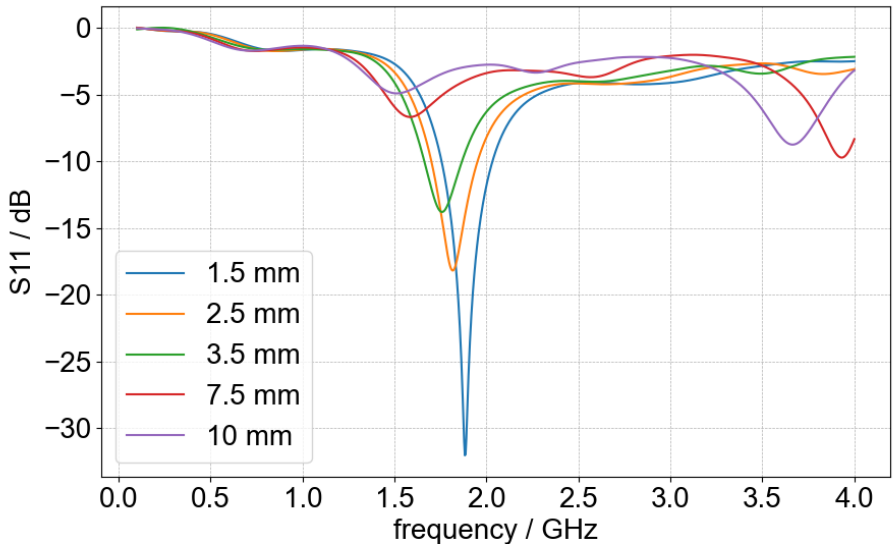

Figure 9. S11 scattering parameter for different PCB thicknesses h.

The radiation properties were evaluated for the modified geometry. The results confirm that the antenna retains the classical “donut” shaped radiation characteristics of a

dipole antenna even at h of 10 mm. The gain performance is slightly exceeding that of the thinner (h=1.5 mm) initial design on certain frequencies.

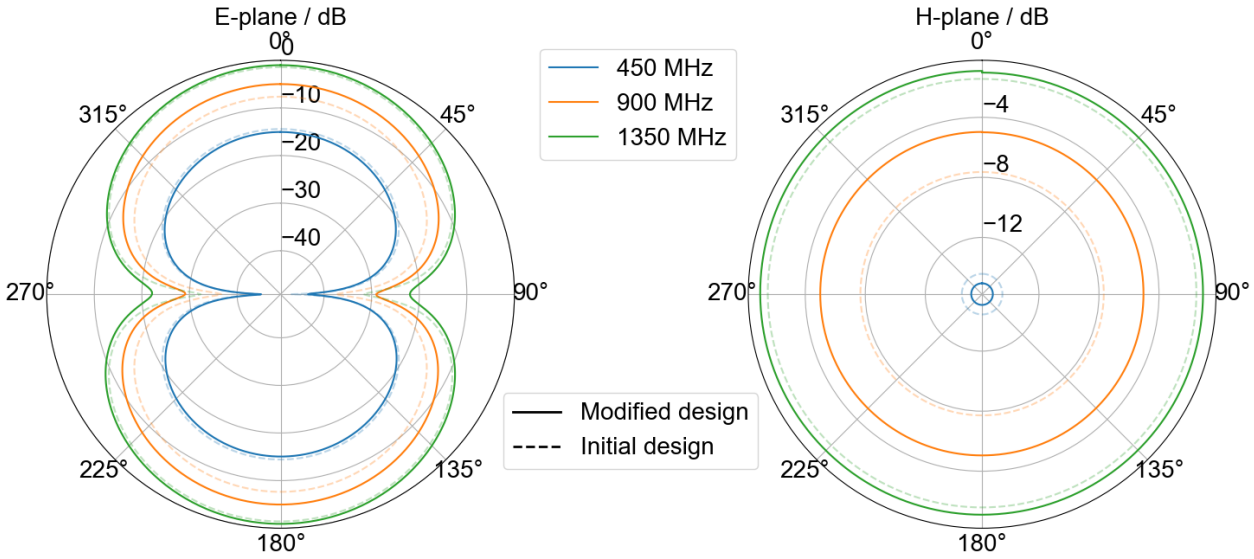

Figure 10. Far-field gain patterns for the antenna with PCB thickness h of 10 mm along with thinner initial design.

3.2.2 Length of the Separation between Poles

Another parameter study was conducted to analyze the influence of the planar geometry on antenna performance. This study focused on the length of the separation l between the elliptical poles and their physical dimensions, in particular, the diameter D_x. The objective was to determine whether these adjustments could shift the operational band to a lower frequency range. For these modified configurations, the width of the PCB substrate was adjusted to accommodate the expanded planar geometry (Figure 11).

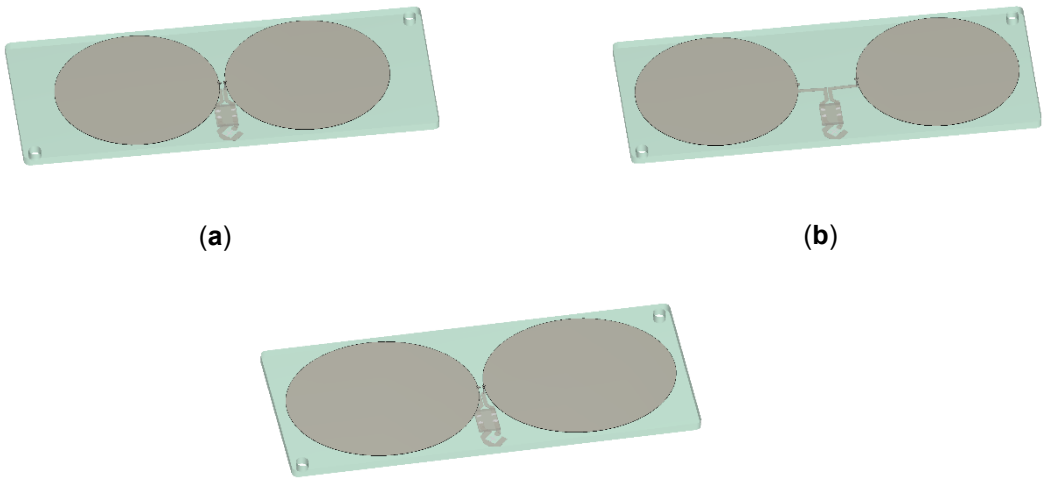

Figure 11. Antenna models: (a) Initial design with separation l=1mm (b) Modified design with l =10mm (c) modified design with l=1 mm and increased diameter D_x=32.7mm.

The effect of varying l on the reflection coefficient S11 is shown in Figure 12. Increasing l results in a downward shift of the resonant frequency. This behavior occurs because the wider separation increases the electrical length of the dipole structure, simulating a physically larger antenna.

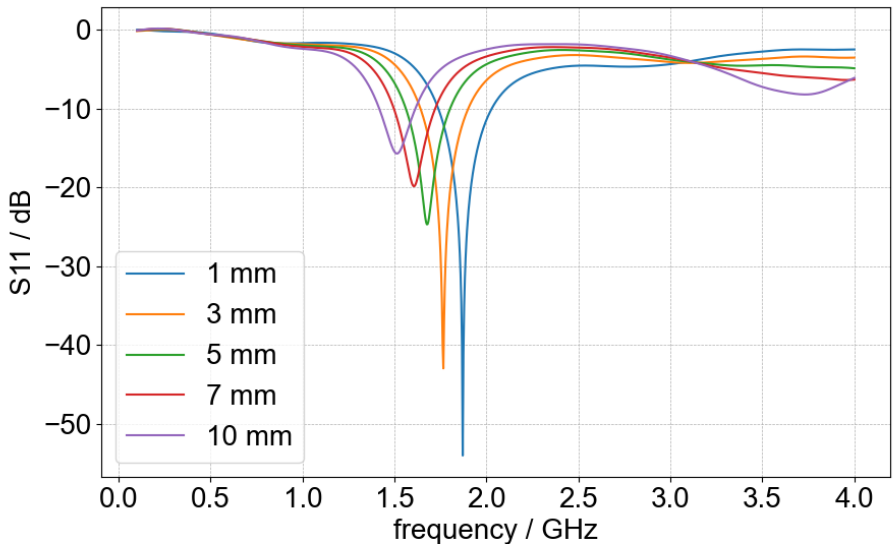

Figure 12. S11 scattering parameter for varying separation l between the elliptical elements.

While increasing l lowers the resonance frequency, it worsens impedance matching. To evaluate this approach, the l =10 mm model was compared against a model where the frequency shift was achieved by increasing the diameter D_x of each of the ellipses by 5 mm. As illustrated in Figure 13, the 10 mm separation results in degradation of the broadband characteristics. This loss of bandwidth is attributed to the weakened coupling between the feed and the radiating elements. Also, the increased distance

between the poles makes it more difficult for electric fields to detach from the antenna structure. In contrast, increasing the diameter results in a deeper resonance below -20 dB and preserves the wideband nature of the dipole on higher frequencies.

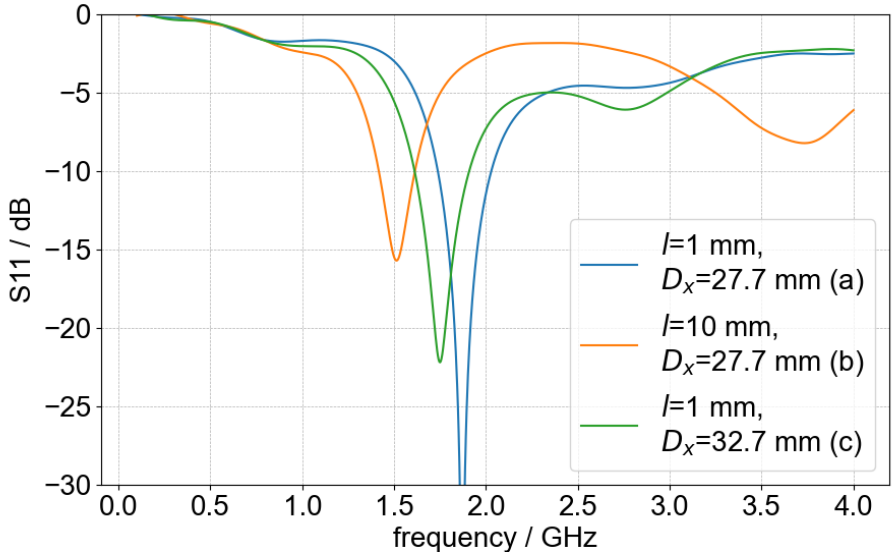

Figure 13. Comparison of S11 performance between the antenna with a large separation l and the antenna with increased element diameter D_x.

Based on the S-parameter analysis, the design with the increased major axis diameter was selected for far-field verification. Figure 14 presents gain patterns for this version compared to the initial design. The scaled antenna preserves the desired radiation pattern and has slightly improved gain across the key frequencies compared to the original smaller design.

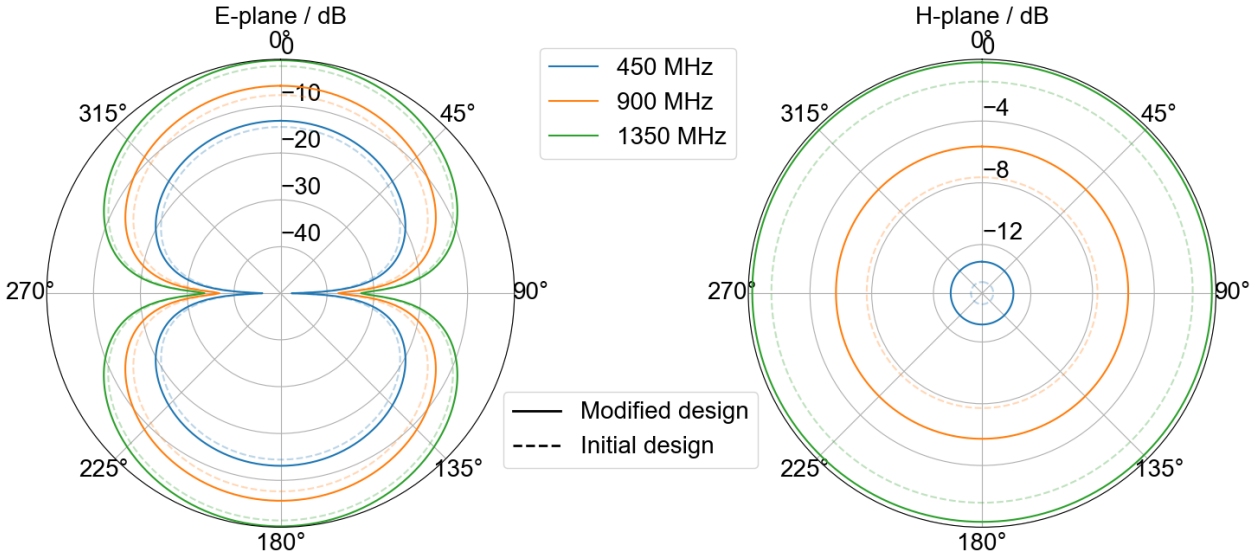

Figure 14. Far-field gain patterns for the antenna with element separation l of 1 mm and diameter D_x of 32.7 mm.

3.2.3 Elliptical Element Dimensions

To evaluate the influence of the elliptical element size and aspect ratio on the center frequency and the bandwidth, a dual-parameter sweep was performed on the diameters: D_x (aligned with polarization) and D_y (perpendicular to polarization) as shown in figure 18. The study varied D_x from 30 mm to 50 mm in 5 mm steps, and D_y in the same range with 10 mm steps. Separation between the elements l was fixed to 1 mm. To accommodate the increased planar area of the larger elements, the substrate dimensions were enlarged to 60 mm x 100 mm. The feed network, including the port and balun configuration on the back side of the PCB, remained unchanged.

The simulated reflection coefficients for the various combinations of D_x and D_y are presented in Figure 15. The results reveal distinct roles of each parameter. As expected, increasing D_x increases the electrical length of the dipole along its polarization axis. This results in a shift of the resonant frequency toward the lower spectrum. For instance, increasing D_x to 50 mm (Figure 15a) shifts the resonance to approximately 1.3 GHz. Variations in D_y primarily influence the profile of the resonance and the bandwidth. For smaller length (D_x = 30 mm), a D_y of 40 mm yields sharpest resonance. Across all configurations, increasing D_y improves the matching performance in the frequency band immediately above the resonant frequency.

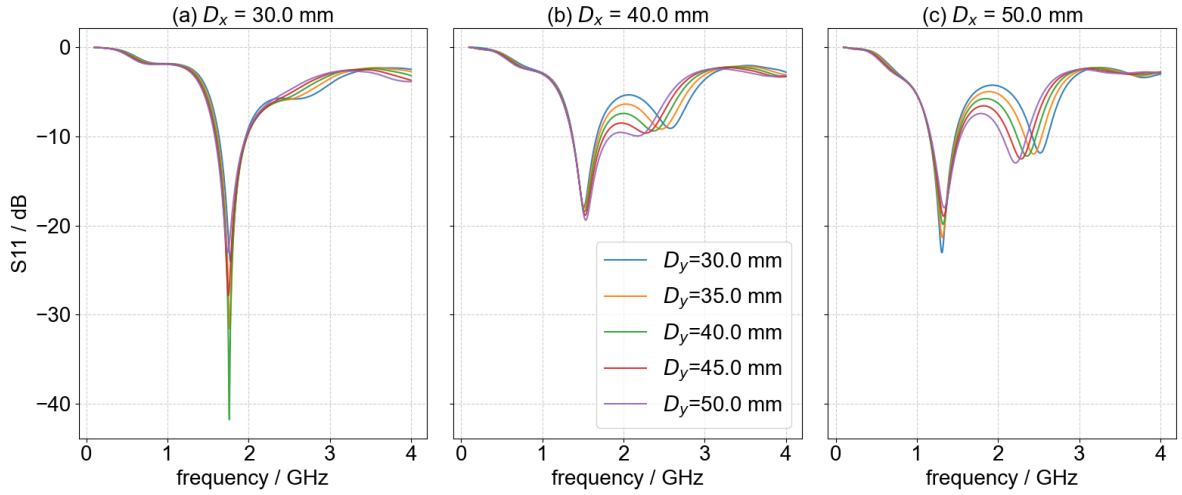

Figure 15. Simulated S11 parameters for varying ellipse diameters.

Even with the largest configuration investigated in this study (D_x = 50 mm), the reflection coefficient at the lower end of the desired operating range (450-1350 MHz) remains above -10 dB. However, the trend clearly indicates that further increase in diameter effectively lowers the operating frequency.

To verify that geometric scaling does not negatively impact radiation patterns, the configuration with the largest dimensions (D_x = D_y = 50 mm) was compared to the initial design. The results confirm that the larger antenna retains the symmetrical dipole radiation characteristics, while offering improved gain performance across the investigated frequencies.

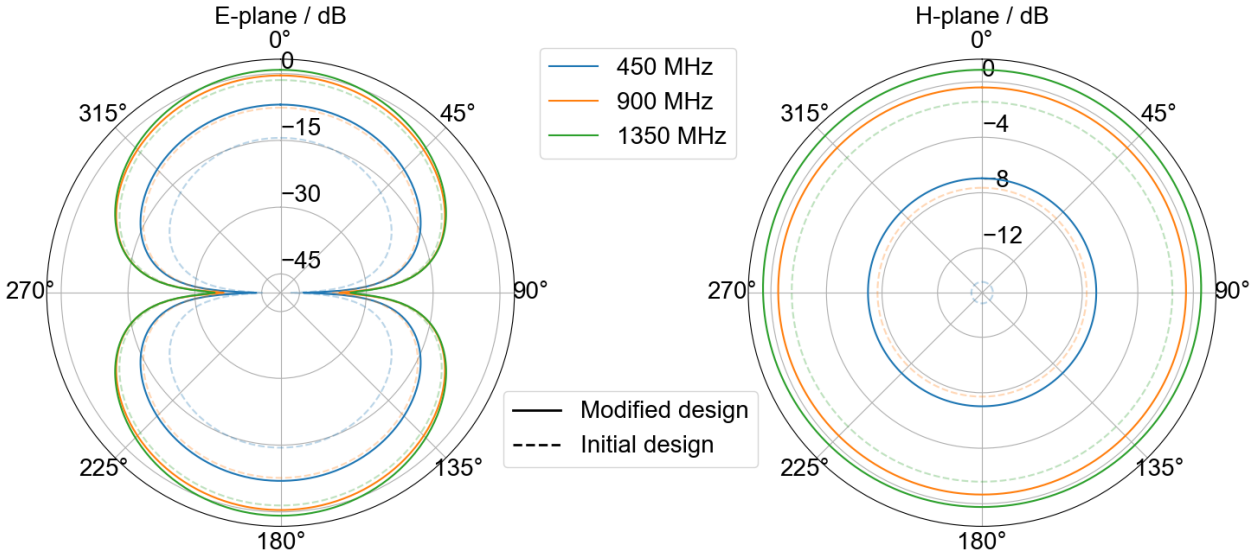

Figure 16. Comparison of polar radiation patterns between the modified antenna (D_x = D_y = 50 mm) and the initial design.

3.3 Optimization of a Larger Antenna

Following the initial parameter study, optimization was conducted to maximize the antenna's performance within the specific mechanical constraints of the deployment environment. The dimensions of the new antenna frame limit the PCB size to - L_{sub}=118.5 mm W_{sub}=58.5 mm. Since a minimum clearance of 1.0 mm between the conductive elements and the PCB edge is required (Figure 2a), the maximum area available for radiating elements was restricted to 116.5 mm x 56.5 mm.

The analysis presented in previous chapters indicated that maximizing the dipole length is required for shifting the operation to the desired lower frequency band. Given the size constraints, full available length of the substrate needs to be utilized. Therefore, rather than varying the horizontal axis diameter D_x and the element separation l independently, the total length was fixed to the maximum available (116.5 mm). D_x can then be expressed as a function of l:

$$Dx = \frac{116.5 - l}{2} \tag{4}$$

This approach reduced the optimization problem to two independent variables: the element separation (l) and the vertical axis diameter (D_y).

To account for the dielectric environment in the operating conditions, the model used during the optimization included the dielectric antenna frame and the lysimeter wall, both defined with a relative permittivity of $\varepsilon_r = 3$. As shown in Figure 17b, the model also accounted for the rectangular cutout required for port connection.

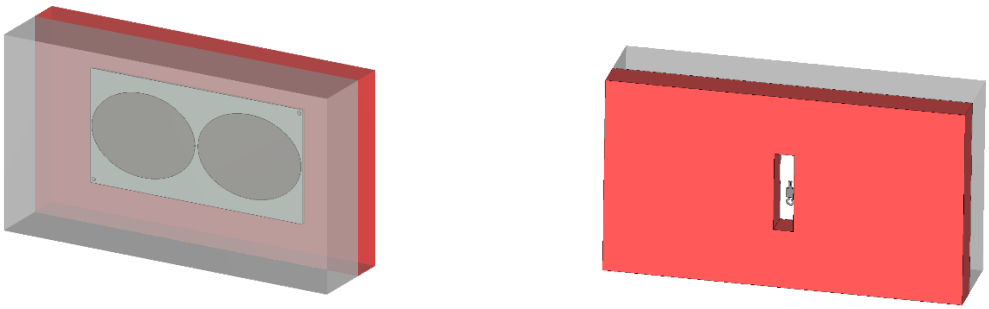

(a) (b)

Figure 17: Simulation model including near-field environment. (a) The antenna is enclosed within the dielectric frame (red) and placed against the lysimeter wall (white) (b) Rear view showing the port access cutout in the frame.

An initial parameter sweep was performed to identify the most promising parameter ranges. l was varied from 1.0 mm to 5.0 mm, and D_y from 32.5 mm to 56.5 mm, both with a step-size of 0.5 mm.

The simulated reflection coefficients (S_{11}) (Figure 18) demonstrate that lower values of D_y result in a sharper, narrowband resonance characteristic, like that of a regular dipole antenna (Figure 1a). Higher D_y values broaden the bandwidth above 1 GHz but provide minimal change in the lower frequency range. Additionally, increasing l (which results in decreasing D_x) shifts the resonance to higher frequencies.

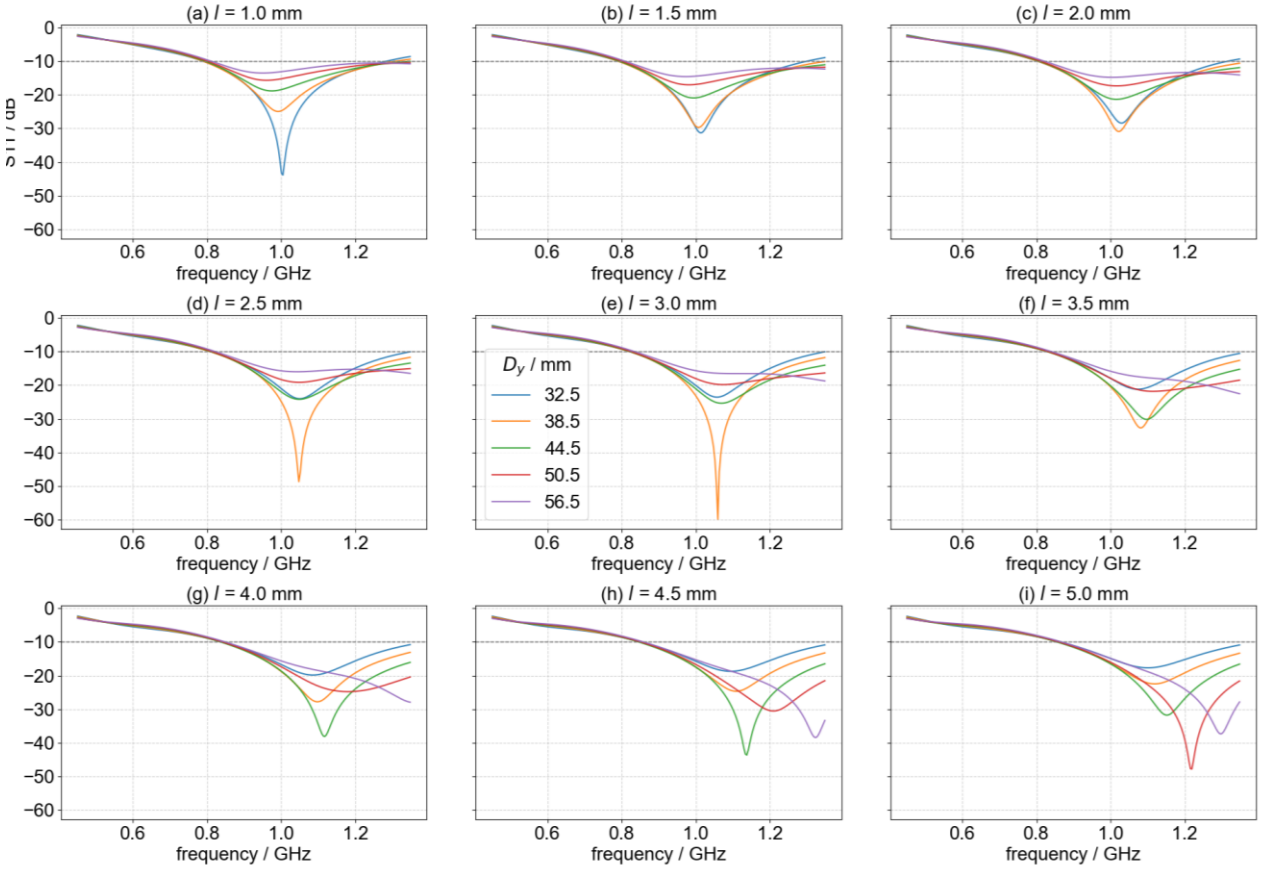

Figure 18: S_{11} results from the coarse parameter sweep. For plot clarity, the displayed step size for D_y is 6 mm.

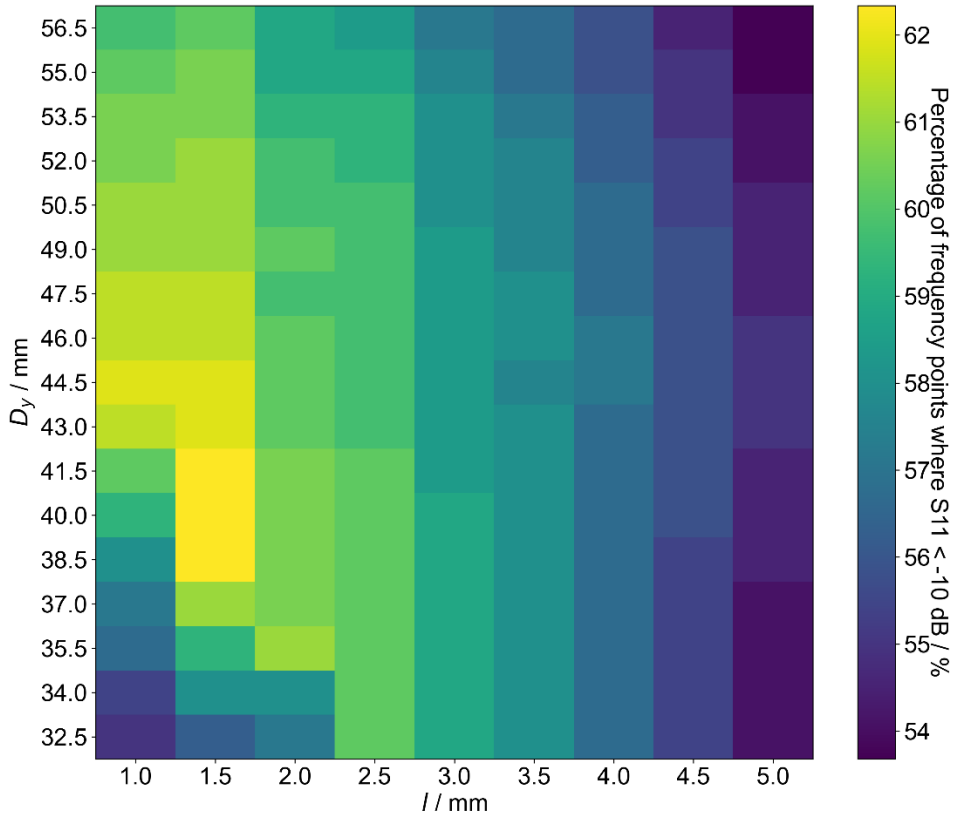

Figure 19: Heatmap of the coverage ratio from the coarse parameter sweep.

To quantify the performance, an evaluation metric was defined as the “coverage ratio”: the percentage of the target frequency band (0.45-1.35 GHz) where S_{11} < -10 dB. The heatmap in Figure 19 illustrates this metric. The optimal region was identified around a separation of 1.5 mm and D_y values between 38.5 mm and 44.5 mm, with a coverage ratio of 62.3%.

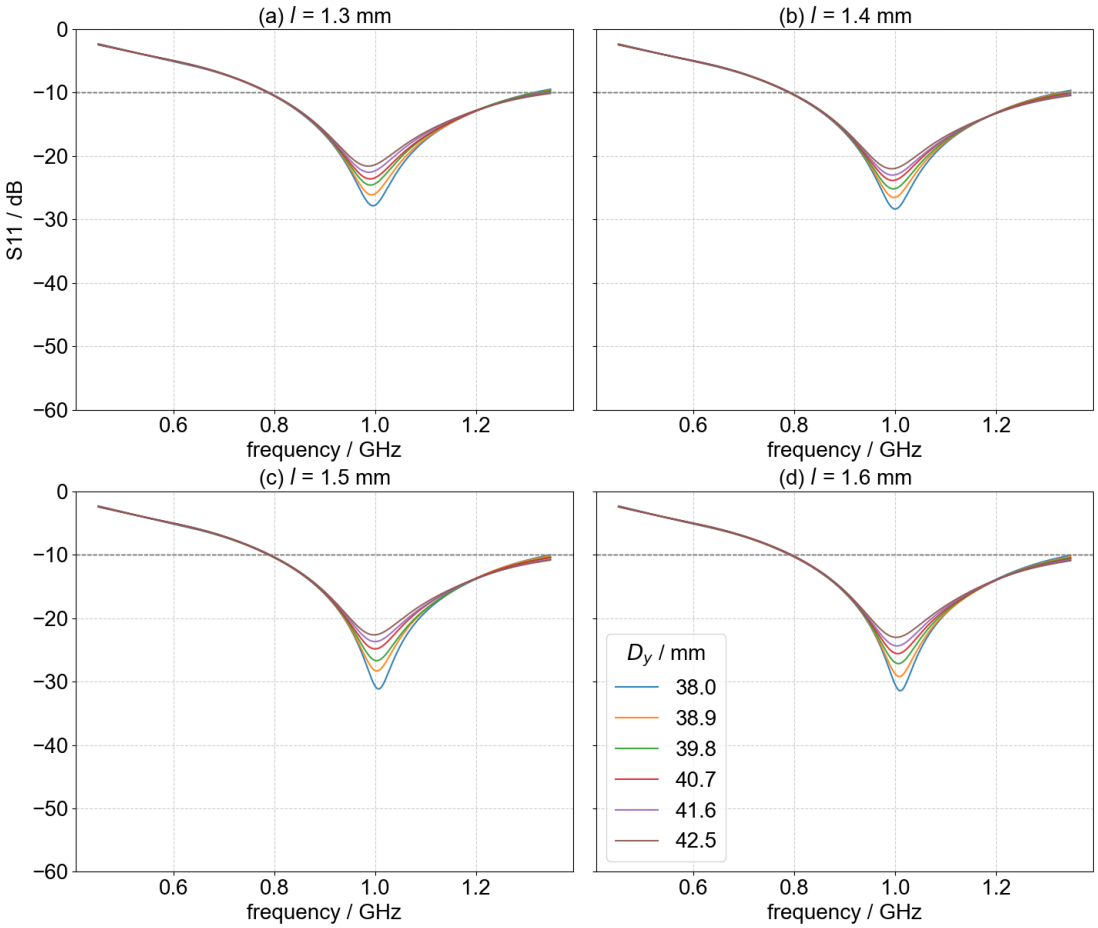

Figure 20: S_{11} results from the finer sweep. Shown D_y step size is increased to 0.9 mm for the clarity of the plot.

Based on the coarse sweep results, a second sweep was conducted with a finer step size of 0.1 mm. The search space narrowed to a new range of 38 to 43 mm for D_y and 1.3 to 1.7 mm for l (Figure 20). The results show a clear correlation between diameter D_y and matching level at the resonance frequency. For lower diameter, matching is stronger. Since the resonance dips are well defined for all parameter combinations in this sweep, a new metric, area under curve for signed-reversed S_{11}, was used for evaluation. Optimal configuration, with l=1.6 mm and D_y=38.2 mm, was identified from the heatmap shown on Figure 21.

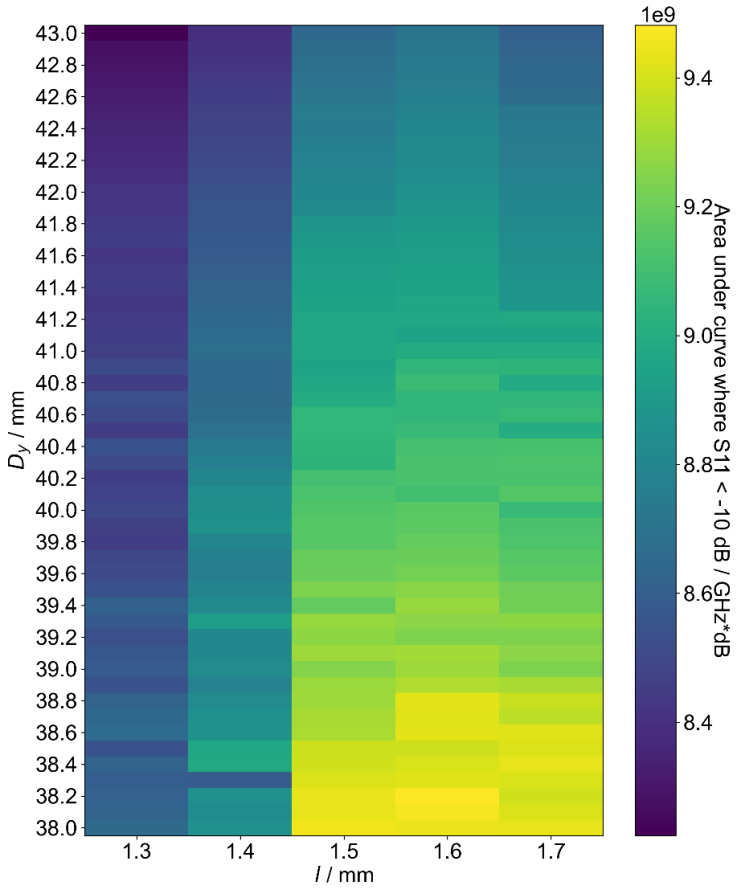

Figure 21: Heatmap of the bandwidth metric from the fine parameter sweep.

The S_{11} curves in different environments for the antenna with optimal configuration are presented in Figure 22. The presence of the dielectric frame and lysimeter wall benefits the design by shifting the resonance to the desired lower frequency and widening the bandwidth. Compared to the original small design (blue curve), the optimized large antenna demonstrates improvement in the target range. The resonance is sharper due to lower aspect ratio (D_y/D_x) in the enlarged geometry.

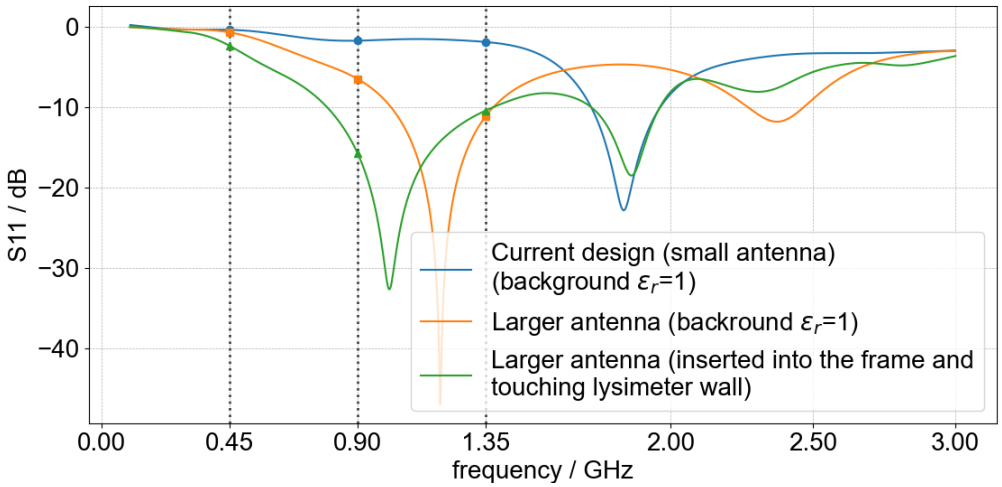

Figure 22: S_{11} comparison of the final optimized design in different environments against the initial small antenna.

Far-field patterns (Figure 23) confirm that the optimized large antenna maintains the dipole characteristics. It also has higher gain compared to the initial design at the key operating frequencies without significant distortion or asymmetry in the E-plane or H-plane.

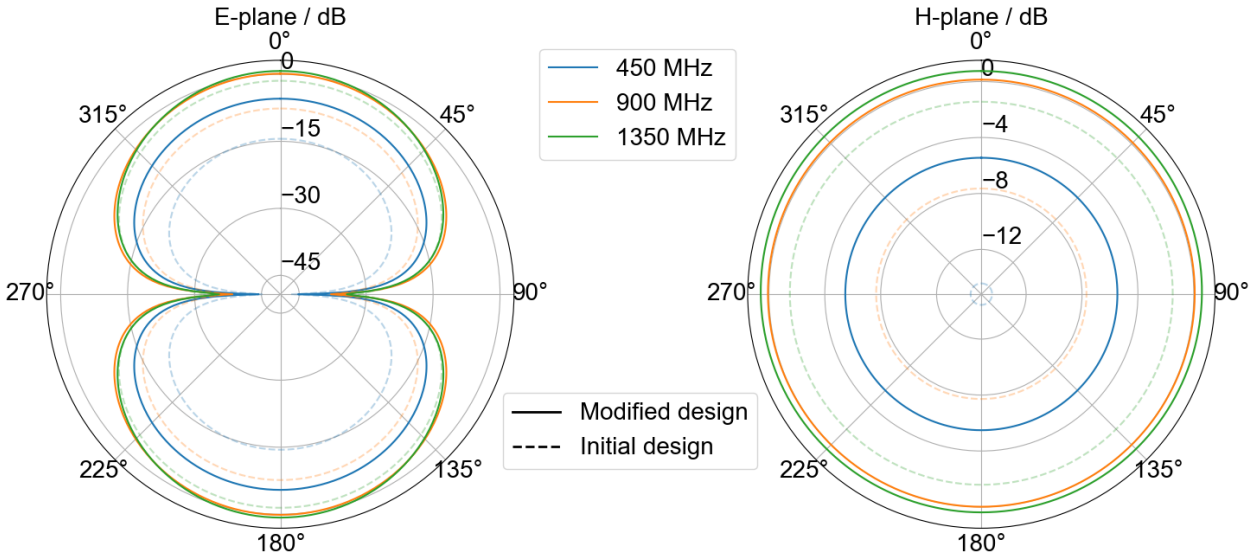

Figure 23: Far-field radiation patterns of the optimized larger antenna compared to the small initial design.

4 Conclusion and Outlook

The paper presented the analysis and optimization of an elliptical dipole antenna for a custom ground-penetrating radar.

The comparison between the simulated results and the scattering parameter measurements demonstrated that the numerical model serves as a reliable digital twin, that opens the possibility of studying and optimizing the antenna behavior under varying geometries.

The initial design shows significant inefficiency within the target operating frequency range of 450-1350 MHz. To address this limitation and develop strategies for tuning the antenna, a sensitivity study was conducted. The analysis yielded insights into the influence of specific design parameters summarized in Table 1.

Table 1. Summary of geometric and environmental parameters on the antenna performance.

Parameter	**Effects on the antenna performance**
Substrate thickness h	Shifts the resonant frequency downward and alters the profile of the curve. Reduces overall matching performance
Ellipse diameter D_x and separation l	Increasing either lowers the center frequency, though they have distinct effects on the shape of the reflection coefficient curve.
Ellipse diameter D_y	Controls bandwidth. Decreasing it sharpens the resonance but reduces the wideband performance.
Environmental dielectric loading	Achieved through introducing the dielectric frame and lysimeter wall ($\varepsilon_r = 3$). They act as a near-field load and shift the resonant frequency downward.

Upon these insights, a scaled-up antenna variant was designed and optimized using brute-force parameter sweep method in the CST Studio Suite. The resulting optimized geometry successfully shifted resonance and achieved a reflection coefficient below -10 dB in the upper half of the operational band.

The next logical step is the fabrication of the optimized larger antenna. New measurements will focus on verification of the new design in our anechoic chamber. To minimize interference from environment, the implementation of a back-shield with the absorbing materials will be investigated.

References

[1] F. Lombardi, B. Ortuani, A. Facchi, and M. Lualdi, “Assessing the Perspectives of Ground Penetrating Radar for Precision Farming,” *Remote Sensing*, vol. 14, no. 23, Art. no. 23, Jan. 2022, doi: 10.3390/rs14236066.

[2] S. Pathirana, S. Lambot, M. Krishnapillai, M. Cheema, C. Smeaton, and L. Galagedara, “Ground-Penetrating Radar and Electromagnetic Induction: Challenges and Opportunities in Agriculture,” *Remote Sensing*, vol. 15, no. 11, Art. no. 11, Jan. 2023, doi: 10.3390/rs15112932.

[3] S. Lambot, E. C. Slob, I. Van Den Bosch, B. Stockbroeckx, and M. Vanclooster, “Modeling of ground-penetrating Radar for accurate characterization of subsurface electric properties,” *IEEE Trans. Geosci. Remote Sensing*, vol. 42, no. 11, pp. 2555–2568, Nov. 2004, doi: 10.1109/TGRS.2004.834800.

[4] T. Kingsuwannaphong, C. Bräu, S. Rümmler, F. Rial, and D. Heberling, “Realistic Railway Ballast FDTD Simulations for Ground Penetrating Radar Railway Track Inspection,” in *2021 11th International Workshop on Advanced Ground Penetrating Radar (IWAGPR)*, Dec. 2021, pp. 1–4. doi: 10.1109/IWAGPR50767.2021.9843175.

[5] S.-E. Hamran *et al.*, “RIMFAX: A GPR for the Mars 2020 rover mission,” in *2015 8th International Workshop on Advanced Ground Penetrating Radar (IWAGPR)*, Jul. 2015, pp. 1–4. doi: 10.1109/IWAGPR.2015.7292690.

[6] A. Novo, R. Sala, M. Kauffman, S. Llobet, P. R. Simon, and M. Arvanitis, “High-resolution GPR investigation over a Roman mosaic in Empuries, Spain,” in *2021 11th International Workshop on Advanced Ground Penetrating Radar (IWAGPR)*, Dec. 2021, pp. 1–5. doi: 10.1109/IWAGPR50767.2021.9843149.

[7] K. Zajícová and T. Chuman, “Application of ground penetrating radar methods in soil studies: A review,” *Geoderma*, vol. 343, pp. 116–129, Jun. 2019, doi: 10.1016/j.geoderma.2019.02.024.

[8] X. L. Travassos, S. L. Avila, R. L. da S. Adriano, and N. Ida, “A Review of Ground Penetrating Radar Antenna Design and Optimization,” *J. Microw. Optoelectron. Electromagn. Appl.*, vol. 17, pp. 385–402, Sep. 2018, doi: 10.1590/2179-10742018v17i31321.

[9] A. P. Annan, “GPR—History, Trends, and Future Developments,” *Subsurface Sensing Technologies and Applications*, vol. 3, no. 4, pp. 253–270, Oct. 2002, doi: 10.1023/A:1020657129590.

[10] C. Ilioudis, “Introduction to Radar Signal Processing”, Accessed: Jan. 30, 2026. [Online]. Available: https://udrc.eng.ed.ac.uk/sites/udrc.eng.ed.ac.uk/files/attachments/Introduction%20Radar%20signal%20processing.pdf

[11] H. M. Jol, *Ground Penetrating Radar Theory and Applications*. Elsevier, 2008.

[12] L. Pajewski, F. Tosti, and W. Kusayanagi, “Antennas for GPR Systems,” in *Civil Engineering Applications of Ground Penetrating Radar*, A. Benedetto and L. Pajewski, Eds., Cham: Springer International Publishing, 2015, pp. 41–67. doi: 10.1007/978-3-319-04813-0_2.

[13] A. Mester *et al.*, “Design of a Novel Scalable Multi-Channel GPR System for High-Resolution High-Speed Tomography of Soil Columns,” presented at the EGU General Assembly Conference Abstracts, Apr. 2025, pp. EGU25-13206. doi: 10.5194/egusphere-egu25-13206.

[14] J. Neumann *et al.*, “The AgraSim (Agricultural Simulator) facility for the comprehensive experimental simulation and analysis of environmental impacts on

processes in the soil-plant-atmosphere system," *EGUsphere*, pp. 1–28, Jul. 2024, doi: 10.5194/egusphere-2024-1598.
[15] A. Klotzsche, H. Vereecken, and J. van der Kruk, "Review of crosshole ground-penetrating radar full-waveform inversion of experimental data: Recent developments, challenges, and pitfalls," *Geophysics*, vol. 84, no. 6, pp. H13–H28, Oct. 2019, doi: 10.1190/geo2018-0597.1.

Jül-4450 • April 2026
ISSN 0944-2952

Mitglied der Helmholtz-Gemeinschaft

JÜLICH
Forschungszentrum